# Flavour-physics benchmarks for tracker-based particle identification at the FCC-ee\*

Anja Beck® and Eluned Smith®

Department of Physics and Laboratory for Nuclear Science, MIT, Cambridge, 02139, MA, USA

(Dated: November 24, 2025)

The correct identification of charged hadrons plays a crucial role in flavour-physics measurements. The final detector configurations at the proposed FCC-ee are yet to be determined and this study aims to contribute to this discussion by benchmarking the particle identification (PID) performance of the proposed CLD and IDEA detectors using fully simulated events. At present, neither detector proposal includes dedicated PID systems, relying instead on information from the tracking subsystems. We estimate the expected level of contamination due to misidentified charged hadrons for b-flavour tagging, rare  $b \to s$  transitions, and s-jet tagging. The PID information provided by silicon trackers, namely time-of-flight and energy-deposit measurements, leads to significant background suppression with high signal efficiency for the low-momentum hadrons considered for same-side bflavour tagging. In order to improve the contamination in rare decays where momenta are in the medium range, only good timing resolution of 30 ps and below can yield an improvement of one order of magnitude below the level achieved by kinematic criteria alone. Light-quark jet-flavour tagging requires identification of particles with very large momentum, which is not possible using only time-of-flight or energy-deposit information in silicon. Access to the number of clusters in a drift-chamber setup, as proposed for the IDEA detector however, results in strong background suppression in every case. This suppression can be further improved in some scenarios by time-of-flight resolution of 30–50 ps or better. The PID quality generally exhibits only a small dependence on the cluster-counting efficiency. Whether dedicated PID detectors could further enhance flavour-physics sensitivity should be the subject of future study.

#### I. INTRODUCTION

The proposed Future Circular Collider (FCC-ee) is designed to provide electron-positron collisions at different centre-of-mass energies in order to determine many parameters of the Standard Model (SM) with unprecedented precision [1]. In particular, experiments at the FCC-ee will be able to measure a range of flavourobservables with world-leading precision: the clean environment will result in significantly higher selection efficiency and smaller systematic uncertainty on measurements of heavy-flavour decays compared to current LHC experiments, while still providing access to the full range of b- and c-hadrons inaccessible at Belle II as well as access to orders of magnitude more data [2]. Also, the flavour reach in the electroweak sector is expected to improve strongly compared to the ATLAS and CMS experiments given the simpler environment and better particle identification (PID).

While the focus and specifications of the detectors is yet to be determined, the composition of high-energy physics detectors mostly follows the same principles. A staple feature in all collider experiments is the tracking system enabling to trace the path of charged particles and their subsequent combination to decay topologies. All modern tracking systems include a silicon vertex-tracker sitting close to the interaction region combined with a second tracking subsystem located further away from the interaction point. The popularity of silicon vertex-detectors can be attributed to their low spatial resolution,

practically instant response time, and the required radiation hardness for elements sitting close to the interaction region of particle beams [3]. The hit resolution can be as low as a few µm as shown for the novel MAPS technology to be implemented in a future upgrade of the ALICE detector [4]. Due to its large material budget and/or cost however, silicon is not a common choice for detectors far from the interaction region. More lightweight solutions are for example drift chambers or time projection chambers

Besides tracking, particle-physics experiments also need to deduce the particle type. This information can be extracted from the signatures that particles leave when traversing different materials. A calorimeter system is crucial for identifying neutral particles, electrons, muons, and charged hadrons based on the total amount of energy deposited and the spatial extent of the deposition. Any measurements related to flavour properties usually require a more granular distinction of charged hadrons into protons, kaons, or pions. Whereas the tracking system provides the momentum of a particle, additional knowledge of its speed allows direct inference of the mass and hence the identity of the particle. Speed can be measured by clocking the time-of-flight along a known path or via the opening angle of a Cherenkov light cone. Similarly, the relationship between either the energy deposited through ionisation or the number of ionisation clusters with a particle speed can enable particle identification. Depending on the overall design and specialisation of a detector, this can be achieved by dedicated particle-identification systems. It may however be convenient and economical to avoid the need for a dedicated subsystem and instead design the tracking system for dual use. Avoiding a dedicated system may also allow

<sup>\*</sup> Contact author: anbeck@mit.edu

for a reduction in the overall material budget of the detector.

This paper presents a study of the charged-hadron identification capabilities of the tracking systems as currently envisioned in the CLD [5] and IDEA [6] detector concepts. The respective tracking detectors and the PID-related quantities obtained from full simulation are presented in Sec. II. Section III outlines the employed particle-identification algorithm. Afterwards in Sec. IV, this tool is applied to three flavour-physics examples in order to determine the expected improvement in contamination for varying levels of time-of-flight resolution and cluster-counting efficiency as well as with and without dE/dx information. This paper concludes with a discussion and summary in Sec. V.

## II. DETECTOR CONCEPTS AND THEIR TRACKING SYSTEMS

The two most mature detector concepts for the FCC-ee are CLD and IDEA. As the name suggests, the CLIClike detector (CLD), described in detail in Ref. [5], was inherited from CLIC studies. Its tracking system is entirely silicon-based and comprises a pixel vertex-tracker as well as two more tracking systems which may use pixels or strips. Ref. [6] provides a detailed description of the other investigated concept named the innovative detector for  $e^+e^-$  accelerators (IDEA). The three tracker subsystems of IDEA are a silicon pixel vertex-tracker, a high-transparency drift-chamber filled with a mix of 90% Helium and 10%  $C_4H_{10}$  gas inspired by the KLOE and MEG2 experiments, and a wrapper using either silicon strips, MAPS, or LGADs. The results obtained from the IDEA studies in this paper can be directly transferred to a third maturing detector concept called a lepton-lepton collider experiment with granular read-out (ALLEGRO) as they share the same tracking system [7]. All studies described in this paper are performed on full simulation of the CLD and IDEA setups using the KEY4HEP framework [8].

The silicon trackers in all detector concepts can provide particle identification by measuring the speed of a particle as the ratio of flight distance over time-of-flight. In this study, the reference points for this measurement are always the first and last recorded hit in any silicon layer. This choice removes uncertainties invoked for particles originating from displaced vertices and does not rely on assumptions regarding the FCC-ee clock resolution. In order to study different values for the time-of-flight precision in the absence of possible improvements due to reconstruction, the true time-of-flight values are smeared using Gaussian distributions. As a consequence, the term time-of-flight resolution in this publication always refers to the magnitude of the  $\sigma$  used in the Gaussian to randomly add noise to the total time-of-flight rather than the timing resolution of an individual pixel. This choice is motivated by the fact that sophisticated tracking algorithms can improve the final time-of-flight resolution for a track significantly relative to the hit-time resolution, see e.g. Ref. [9]. The uncertainty imposed on the flight distance by the finite size of each pixel is naturally included in this study as the hit location is taken from the output of full simulation. Tracking and clustering algorithms can also improve this spacial uncertainty but it is already so small that the impact on the study at hand is negligible.

Another useful quantity for particle identification is the energy-deposit per travelled distance, dE/dx, in each silicon sensor. The ability of the detector to measure the energy deposit is assumed to be modelled realistically in the simulation and used without additional smearing. Inspired by CMS studies, the dE/dx value per track is determined as the harmonic mean with grade -2 of all recorded hits in silicon layers [10].

Finally, the drift chamber in the IDEA concept also allows for a measurement of the number of primary ionisation clusters per travelled distance, dN/dx. Because the number of clusters follows a Poissonian distribution instead of a Landau distribution, dN/dx is preferred over dE/dx, which can also be measured with a drift chamber. The number clusters is not yet available in the IDEA simulation but instead extrapolated based on Garfield simulations [11] while the travelled distance is taken from simulation without modification. The extrapolated value for the number of clusters in each cell is varied according to a Poissonian. The dN/dx value per track is obtained by adding the number of clusters in all cells and dividing by the total distance. In order to study the impact of different cluster-counting efficiencies later on, each cluster is kept or discarded stochastically with a probability corresponding to the chosen efficiency.

Figures 1 and 2 show the dependence of these particle identification quantities on the momentum for proton, kaon, and pion tracks in the two detector concepts. Because no full tracking algorithm is yet available for the IDEA detector, the generated momentum is used for both IDEA and CLD studies. Given that a momentum resolution well below 1% in the momentum range  $p < 100\,\mathrm{GeV}/c^2$  is achievable even for the much more complex events at the LHC [12], this choice has negligible impact on the results.

In order to have a dE/dx or dN/dx measurement, a track needs at least one hit of significant energy in a silicon sensor or the drift chamber. A timing measurement on the other hand requires at least two hits in the silicon detectors. The gray points in the figures correspond to tracks which lack at least one of these measurements. This is particularly striking for the dE/dx and speed measurements in IDEA, see the top and middle plots in Fig. 2, because a sizeable amount of tracks does not have a dN/dx measurement. The two main reasons for the lack of dN/dx information are 1) the available interpolation to calculate the dN/dx values is only valid for  $\beta\gamma \geq 0.5$  and 2) the silicon detectors in IDEA and CLD have further acceptance reach towards the beam

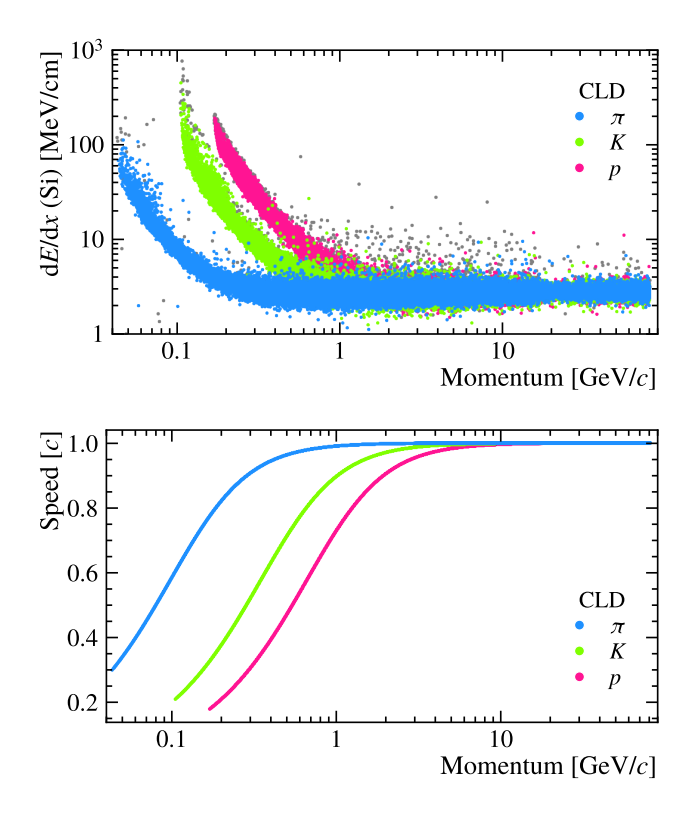


FIG. 1. Input quantities for particle identification using CLD tracking detectors. Top:  $\mathrm{d}E/\mathrm{d}x$  in the silicon sensors, calculated as the harmonic mean of all hits in silicon trackers. Bottom: speed measured using the time-of-flight and flight-distance between the first and the last hit in silicon trackers.

pipe compared to the drift chamber. Tracks without any usable measurement are discarded from the study.

# III. PARTICLE IDENTIFICATION ALGORITHM

We employ boosted decision trees (BDTs) to determine the identity of a particle because they are able to capture high-dimensional correlations while providing high interpretability, effectively producing a non-trivial binningscheme across all input variables. The training events are individual particles generated isotropically ensuring sufficient balance between protons, kaons, and pions as well as full coverage of the angular space. For each charge and species, 100 000 events are produced, resulting in a total of 600 000 training particles. The three flavour-physics examples considered later stem from  $e^+e^- \rightarrow Z \rightarrow b\bar{b}$ and  $e^+e^- \to Z(\to \text{anything})H(\to \text{light quarks})$  events. Given that particle identification relies heavily on the momentum of a particle, the particle-gun training-samples are generated in 20 bins of equal content defined based on the momentum distribution of the  $e^+e^- \to ZH$  events considered later. Within each bin, the momenta are distributed uniformly. The ZH events are chosen as they

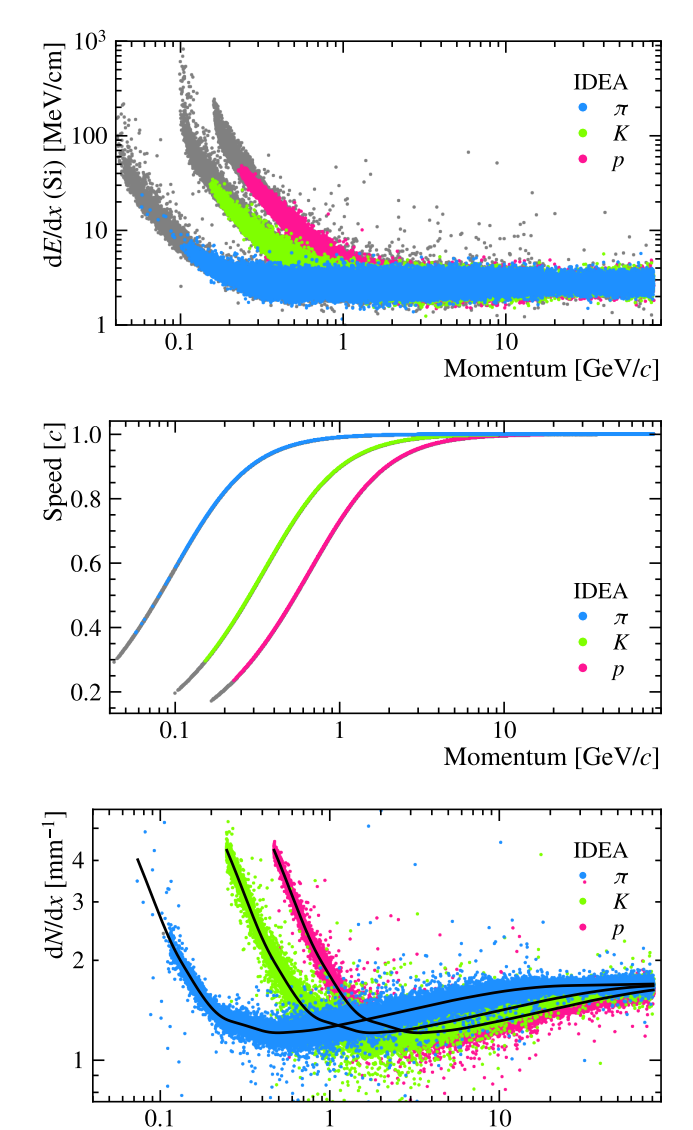


FIG. 2. Input quantities for particle identification using IDEA tracking detectors. Top: dE/dx in the silicon sensors, calculated as the harmonic mean of all hits in silicon trackers. Middle: speed measured using the time-of-flight and flight-distance between the first and the last hit in silicon trackers. Bottom: dN/dx interpolated from GARFIELD simulation (black line) with Poissonian variation at the generation stage (dots).

Momentum [GeV/c]

have a broader momentum profile. Figure 3 illustrates the momentum distribution of the charged hadrons for different event types and the particle-gun samples.

The particle-gun events are propagated through full GEANT4 simulation of both the IDEA and CLD detector concepts [13–17]. The BDTs are trained on 80% of the particle-gun samples and the remaining 20% are kept for validation. In order to achieve similar magnitudes of the features, the speed v is scaled using  $\log(1-\frac{v}{c})$  and the energy-deposit dE/dx is scaled using  $\log(dE/dx)$  before

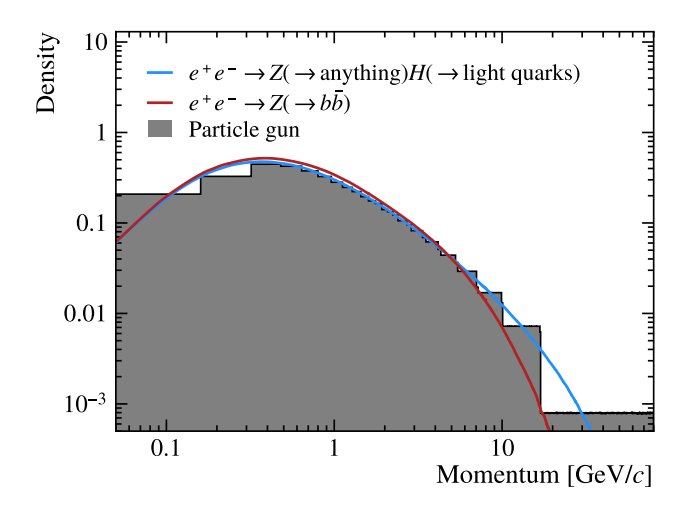


FIG. 3. Generator-level distributions of the charged-hadron momenta in the samples used to study specific flavour measurements and the particle-gun samples employed for training the classifiers.

training the BDTs.

The particle-identification algorithm consists of three independent BDTs trained to select protons, kaons, or pions over the other two species. For an unseen particle, the species is assigned according to the BDT with the highest output score. In order to avoid over-fitting, the depth of each BDT is limited to the number of training features in the given setup and in each boosting step only 80% of the training set are used. All other parameters are set to the default values used by the python implementation of XGBOOST as the performance is not very sensitive to reasonable changes in the hyperparameters [18].

The left column of plots in Fig. 4 shows the receiver-operator curves (ROCs) for different time-of-flight resolution (indicated by colour) at CLD calculated on the unseen particle-gun validation samples. The coloured lines represent BDTs that use the energy deposit in the silicon trackers. For each coloured line, there is a corresponding gray line which represents the same setup but without dE/dx information. For large time-of-flight resolutions, the additional dE/dx input improves the AUC notably while it has negligible impact for better time-of-flight resolution. Even the poorest considered time-of-flight resolution of 500 ps leads to AUC values significantly larger than 0.5.

The right column in Fig. 4 shows the same set of plots but for IDEA with a cluster-counting efficiency of 80%. Comparing the coloured lines between the CLD (left) and IDEA (right) performance reveals that the additional dN/dx information improves the classification. Note that the black lines representing a scenario without time-of-flight measurement reaches a similar AUC as relying on a time-of-flight measurement of 10 ps for pion identification (purple line in the CLD plot). For all setups, proton and pion identification achieves higher AUCs than kaon

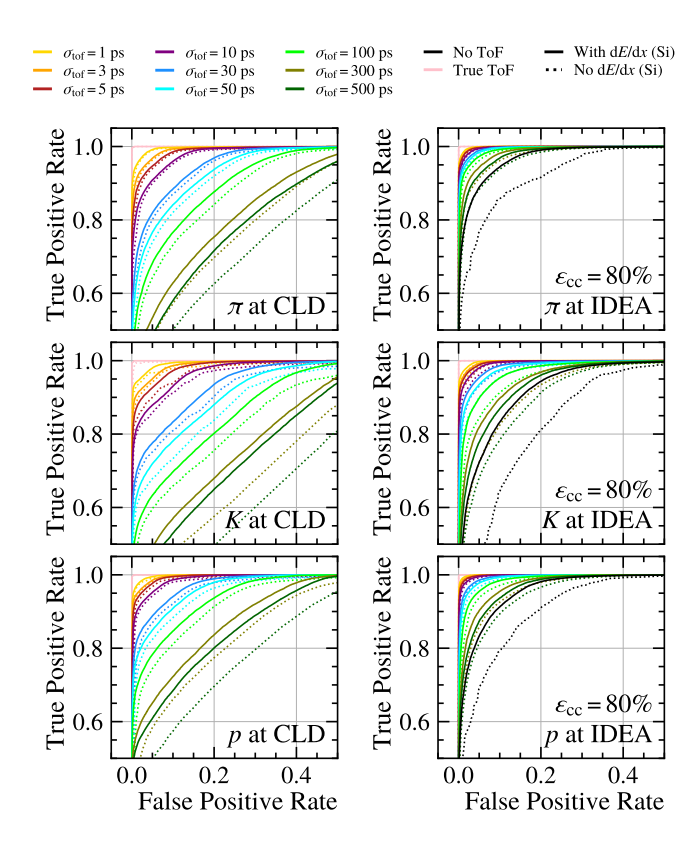


FIG. 4. (Left/right) ROC for the (top) pion, (middle) kaon, and (bottom) proton identification at CLD/IDEA. The colours indicate the time-of-flight (ToF) resolution and the linestyle indicates whether the silicon-based dE/dx information was used. A cluster-counting efficiency  $\varepsilon_{cc}$  of 80% is assumed for the drift-chamber reconstruction at IDEA.

identification because in the latter case outliers in both directions lead to misidentification compared to only one direction for protons and pions.

Figure 5 shows the dependence of the AUC on the particle momentum. While identification in the very low momentum regime is close to perfect in almost any setup, the cluster-counting information at IDEA leads to strong particle-identification performance even at higher momenta. The dips in the IDEA AUC scores at medium momentum are a consequence of the crossing between the dN/dx curves as shown in the bottom part of Fig. 2. The theoretical dE/dx shapes intersect in the same way which is not visible in Figs. 1 and 2 due to finite resolution and the lack of density information in the scatter plot. Despite the dilution, this effect is slightly visible for CLD and poor time-of-flight resolution. At 500 ps for example (dark green lines), adding dE/dx information (solid line) on top of pure time-of-flight classification (dotted line) increases the AUC score visibly at low and high momenta while the improvement is only moderate in the 1-3 GeV/c region.

The dependence on the cluster-counting efficiency is generally rather low as the classifier simply learns the additional scaling. Appendix A shows the information in

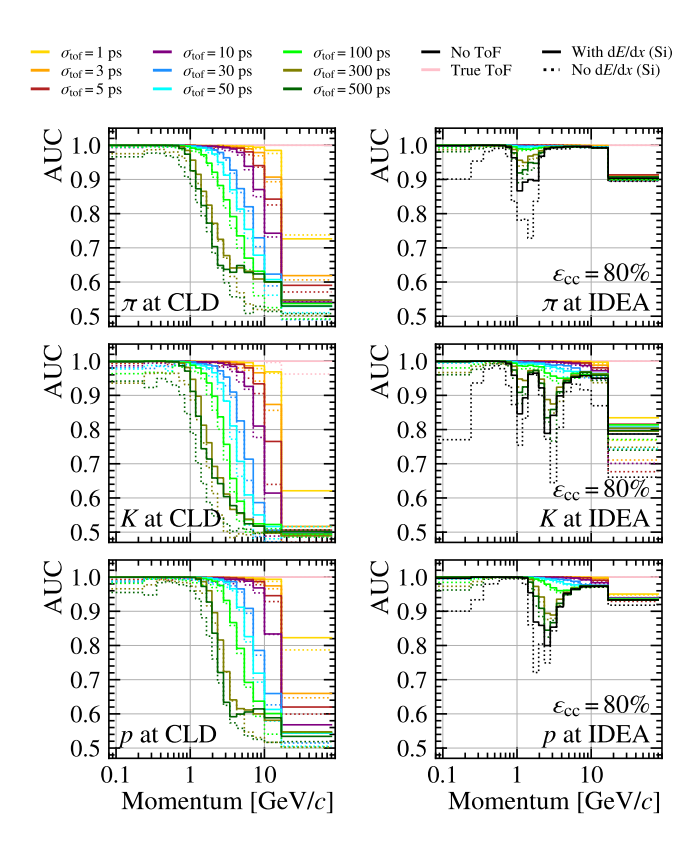


FIG. 5. (Left/right) AUC in different momentum ranges for the (top) pion, (middle) kaon, and (bottom) proton identification at CLD/IDEA. The colours indicate the time-of-flight (ToF) resolution and the linestyle indicates whether the silicon-based dE/dx information was used. A cluster-counting efficiency  $\varepsilon_{cc}$  of 80% is assumed for the drift-chamber reconstruction at IDEA.

Figs. 4 and 5 for cluster-counting efficiencies of 50% and 100%.

To represent the performance of a particle-identification tool, the fraction of misidentified particles, f, is converted into a number of standard deviations,  $\sigma$ , using

$$f_{\sigma} = \Phi^{-1}(1 - f) ,$$
 (1)

where  $\Phi$  is the cumulative distribution function of the normal distribution. We choose not to explicitly quote a separation power, as the BDT responses are non-Gaussian. However the separation of the BDT discriminator distributions for different particle species can be judged by eye from the plots in App. B for a few example configurations. Figure 6 shows the level of misidentification for all combinations of particle species for the different configurations tested on CLD (i.e. time-of-flight measurement with or without dE/dx measurement). As expected, the misidentification is low at very low momenta where the distance between the speeds for the different particle types is rather large. For most particle combinations, including dE/dx information from the silicon tracker (left column) improves the differentiation

at low momentum regardless of time-of-flight resolution and at medium momentum in the case where time-of-flight is only known with a precision of 100 ps or worse. Interestingly at very high momenta, dE/dx information deteriorates the classification presumably due to the additional noise without distinction power, see top parts of Fig. 1. Note that 10 000 particles per species are considered in each bin. In case none of the 10 000 particles in the given bin was misidentified, the lower limit of the 68% confidence level on  $f_{\sigma}$ , sitting at around 3.7 $\sigma$ , is shown.

Figure 7 shows the same set of plots for the IDEA case (i.e.dN/dx measurement with or without time-of-flight and/or dE/dx measurement) with a cluster-counting efficiency of 80%. The dependency on the cluster-counting efficiency is limited and equivalent figures for 50% and 100% can be found in App. A. Considering the configuration without time-of-flight measurement represented by the black lines shows that the particle identification performance for all particle combinations is high at very low momentum, drops between 1 GeV/c and 3 GeV/c depending on the mass difference of the particles, and rises again at higher momentum. This behaviour is expected and mirrors the shape of the dN/dx curves shown in the bottom plot of Fig. 2. As discussed earlier, this behaviour is also reflected in the variation of the AUC score with momentum shown in Fig. 5. The severity of the drop between 1 GeV/c and 3 GeV/c has a slight dependence on the cluster-counting efficiency, see App. A. The addition of a time-of-flight measurement (all other colours) mitigates the aforementioned drop once the precision reaches 10–30 ps. At very low momentum, time-of-flight information of any precision improves the performance. Alternatively, measuring dE/dx on top of dN/dx but without time-of-flight (black lines, left plots) also achieves low misidentification rates at very low momentum.

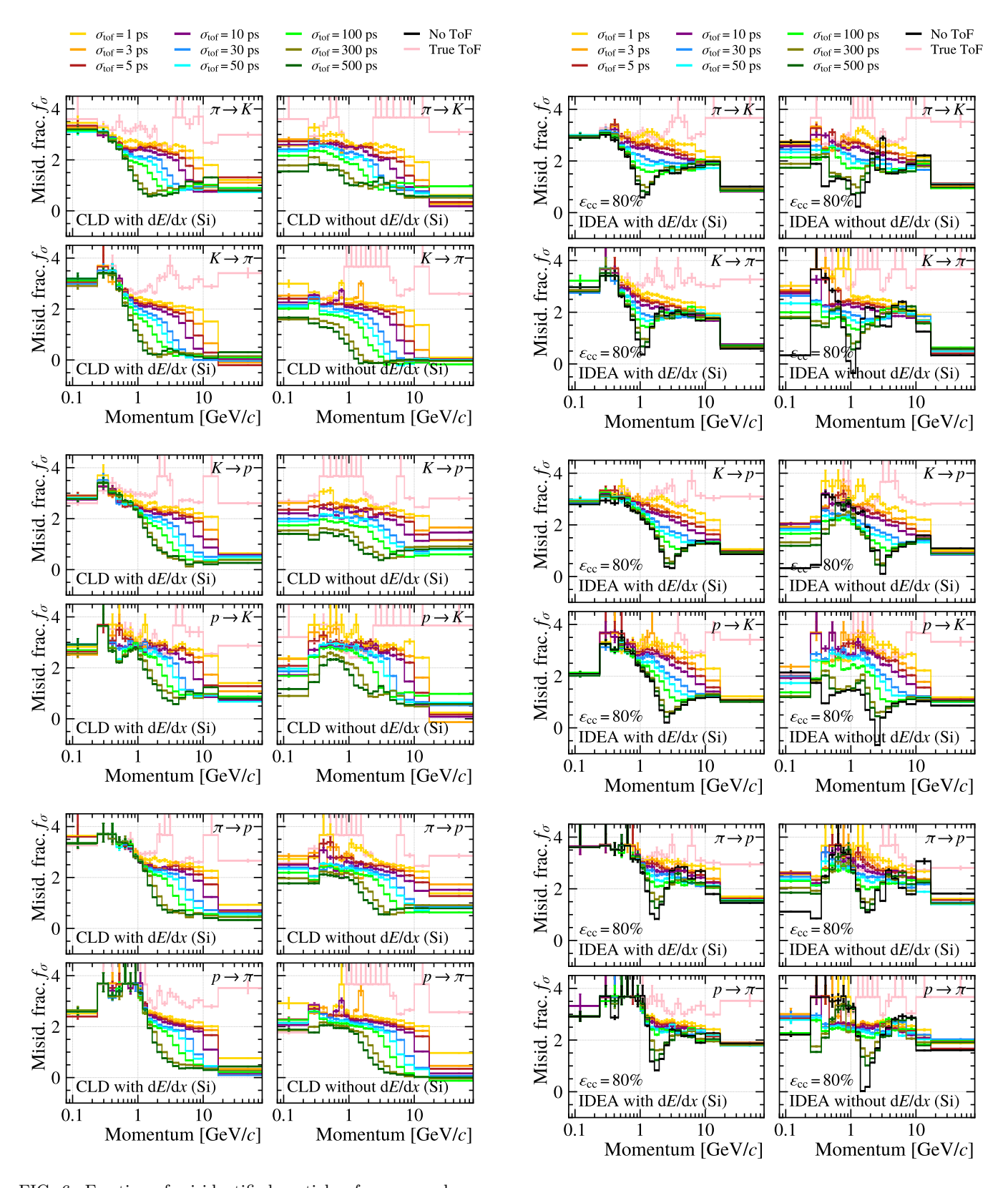


FIG. 6. Fraction of misidentified particles  $f_{\sigma}$  expressed as a number of standard deviations using Eq. (1) for each combination of hadron species (top, middle, bottom) for different time-of-flight (ToF) resolution and without (left) and with (right) dE/dx information at CLD (*i.e.* time-of-flight measurement with or without dE/dx measurement).

FIG. 7. Fraction of misidentified particles  $f_{\sigma}$  expressed as a number of standard deviations using Eq. (1) for each combination of hadron species (top, middle, bottom) for different time-of-flight resolution (ToF) without (left) and with (right) dE/dx information at IDEA (i.e.dN/dx measurement with or without time-of-flight and/or dE/dx measurement). A cluster-counting efficiency  $\varepsilon_{\rm cc}$  of 80% is assumed.

# IV. APPLICATION TO EXAMPLE FLAVOUR-PHYSICS MEASUREMENTS

This section illustrates the reduction in contamination achieved through tracker-based particle-identification for three example physics-cases. For each example, both CLD and IDEA are considered using configurations with different values for the time-of-flight resolution, the cluster-counting efficiency, and with or without siliconbased dE/dx information. The three examples study (A) the signal and background efficiency for tagging the b-flavour of  $B_s^0$  mesons based on same-side tagging using the net number of charged kaons produced alongside the  $B_s^0$  meson in the hadronization process, (B) the contamination due to hadron misidentification in fully visible and the semi-visible rare decays, and (C) the signal and background efficiency when discriminating s-jets against jets from other light quarks based on the charged hadron with the highest momentum in the jet. Figure 8 illustrates how these three examples test vastly different momentum ranges.

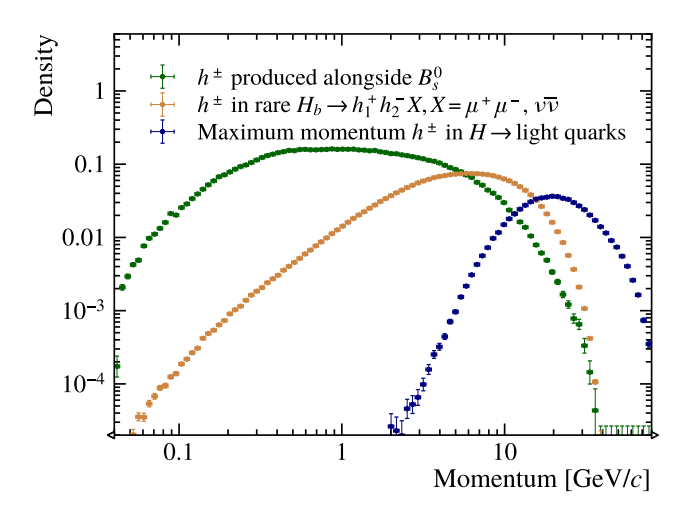


FIG. 8. Momentum distributions of the charged hadrons considered in the three example flavour physics cases.

# A. b-flavour tagging

Neutral b-mesons can oscillate between their particle and antiparticle states. Knowledge of the exact meson state at production plays an important role in the flavour sector allowing access to time-dependent and additional CP-violating amplitudes, see e.g. Ref. [19]. The sensitivity is particularly large for  $B_s^0$  decays given the small difference between mass eigenstates.

The FCC-ee running at the Z pole produces  $b\bar{b}$  pairs flying back-to-back in the lab frame. A number of additional, typically lighter, hadrons are produced in the hadronization process. Because the strong force is

flavour-conserving, the flavour of the b-quark can be identified by the lighter hadrons produced alongside. For example, the b-quark might hadronize to a  $\overline{B}_s^0$  meson with the  $\overline{s}$ -quark produced via an  $s\overline{s}$  pair from the vacuum. The additional s-quark must hadronize too leading to a negatively charged or neutral kaon. This type of tagging is usually referred to as a same-side tagger.

The b-quark might also be identified through first identifying the  $\bar{b}$ -hadron on the other side of the event. This procedure is typically called an *opposite-side tagger* and relies on identifying the  $\bar{b}$ -hadron based on its decay products. Due to excellent expected mass resolution at the FCC-ee, this is likely possible without employing particle-identification tools. As a consequence, the opposite-side tagger is not investigated here.

Modern b-flavour tagging algorithms employ machine-learning tools to decipher the multidimensional correlations that provide the most efficient tag, see e.g. Refs. [20–23]. Developing such an algorithm for the FCC-ee environment reaches beyond the scope of this study. Instead, the investigations focus on the simplest case, tagging  $B_s^0$  and  $\overline{B}_s^0$ , using the previously discussed proxy, the net number of kaons. This means that a b-hadron is tagged as  $B_s^0$  if it is accompanied by a larger number of  $K^+$  than  $K^-$  in its hemisphere and vice-versa for the  $\overline{B}_s^0$ . Accounting for the detector acceptance, this classification would catch 45% of the  $B_s^0$  and  $\overline{B}_s^0$  mesons if perfect particle identification were possible.

Figure 9 shows the resulting tagging efficiency to correctly identify a  $B_s^0$  meson in red and corresponding mistag efficiency in blue. The efficiencies are calculated wrt. the 45% of  $B_s^0$  with more  $K^+$  than  $K^-$  that can be identified this way in order to show the efficiency improvement through particle identification rather than the efficiency of the algorithm. As a consequence of the very low momentum of the considered particles, see Fig. 8, a moderate tagging efficiency can be achieved for timeof-flight resolution below 50 ps at CLD. The addition of dE/dx information is only beneficial for time-of-flight resolution above 100 ps. While the trends are fairly similar, IDEA consistently achieves significantly better performance for time-of-flight resolutions in the most realistic range between 30 ps and 100 ps almost regardless of cluster-counting efficiency.

#### B. Rare decays

Precision measurements of electroweak-penguin decays of b-quarks provide sensitivity to effects at energy scales beyond the direct reach of current or future colliders. Measurements of  $b \to s \ell^+ \ell^-$  transitions in different hadronic systems indicate tensions between measurement and prediction [24–44]. Strong suppression of background is crucial to achieve high precision in rare-decay measurements. This is particularly important in angular analyses where the contribution from misidentified rare decays with their unique angular distributions can bias

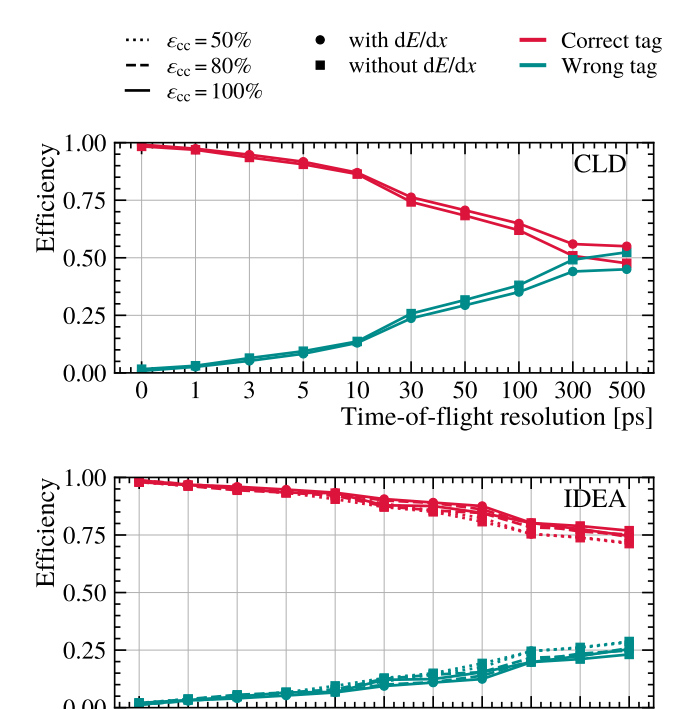


FIG. 9. Efficiency of (mis)tagging  $B_s^0$  mesons by requiring that more  $K^+$  than  $K^-$  are produced alongside the  $\bar{b}$ -meson for CLD (top) and IDEA (bottom) for different time-of-flight resolution (horizontal axis), different cluster-counting efficiencies  $\varepsilon_{cc}$  (IDEA only, distinguished by linestyle), and with or without using energy-deposit information from the silicon sensors (markerstyle).

30

5

3

0

50 100 300 500

Time-of-flight resolution [ps]

the result. Moreover, this bias is hard to quantify because the background distribution itself is often not well known such that background suppression is the only viable option.

The examples considered in this study are the three hadronic systems  $B_s^0 \to K^+K^-, B^0 \to K^-\pi^+,$  and  $\Lambda_b^0 \to p K^-$  either with two muons of opposite charge or a neutrino-antineutrino pair. The b-hadrons are produced using Pythia in  $e^+e^-$  collisions at the Z pole [45]. They are decayed by the EVTGEN package forcing a uniform distribution in the dilepton invariant-mass squared [46]. The compositions of the dihadron spectra are inspired by previous analyses at the photon or  $J/\psi$  pole [47–49] with details in App. C. The production fractions used to calculate the contamination are  $f_{B^0} = 0.407$ ,  $f_{B_s^0} = 0.101$ , and  $f_{\Lambda_b^0} = 0.075$  [50]. The  $\Lambda_b^0$  hadronization fraction is an estimate based on the measured hadronization fraction to any b-baryon of 0.085 [50] and the assumption that 89% of b-baryons are  $\Lambda_b^0$  baryons, 10% of b-baryons are neutral or charged  $\Xi_b$  baryons and 1% are other bbaryons [51]. The decay branching fractions are set to be equal.

#### 1. Fully-visible final-states

For fully-visible final-states, the four-body invarianthelpful discriminator between different b-hadrons. When considering for example  $B_s^0 \to K^+ K^- \mu^+ \mu^-$  as the signal decay, the four-body invariant-mass of true signal candidates accumulates in a peak at the nominal  $B_s^0$  mass. The shape and width of the peak are a consequence of the resolution of the tracking system and reconstruction algorithm. Previous studies of fully-visible muonic rare decays using fast simulation of the IDEA detector showed invariantmass peaks with a full-width at half-maximum around  $\begin{array}{lll} 10\,{\rm MeV}/c^2 & {\rm for} & B_s^0 \to \phi(\to K^+K^-)\mu^+\mu^- & {\rm decays} & [52], \\ 8\,{\rm MeV}/c^2 & [53] & {\rm for} & \Lambda_b^0 \to \Lambda(\to \ p\pi^-)\mu^+\mu^- & {\rm decays}, \ {\rm and} \\ 4\text{-}5\,{\rm MeV}/c^2 & [54] & {\rm for} & \Lambda_c^+ \to p\mu^+\mu^- & {\rm decays}. \ {\rm Reference} & [1] \end{array}$ provides similar values for other decays. Misidentified backgrounds on the other hand appear in very broad smeared-out structures in the signal invariant-mass, which are stretched across several  $\text{GeV}/c^2$  in the FCC-ee setting. See App. D for an illustration.

The narrow signal peaks and the wide spread of backgrounds allow to efficiently select signal and suppress background by focusing on narrow windows around the signal b-hadrons (i.e. the  $B_s^0$  mass region in the  $KK\mu\mu$ combination for a  $B_s^0$  signal) while vetoing narrow windows around the background b-hadrons (i.e. the  $\Lambda_b^0$  mass region under the  $pK\mu\mu$  hypothesis as well as the  $B^0$  mass under the  $K\pi\mu\mu$  hypothesis). Because the four-body invariant-mass in this study is obtained from the true momenta, different values for the resolution are added artificially by smearing the four-body invariant-mass with a Gaussian of predetermined width. The results shown in the main part of this paper use a Gaussian distribution with  $\sigma = 5 \,\mathrm{MeV}/c^2$  which translates to a conservative full-width at half-maximum of  $11-12 \,\mathrm{MeV}/c^2$ . The window for selecting signal and vetoing background peaks is  $\pm 10 \,\mathrm{MeV}/c^2$  around the nominal peak mass. For this configuration and considering the  $B_s^0$  decay as signal, the chosen kinematic constraints have an efficiency of 73.8%/0.2%/0.1% for the  $B_s^0/B^0/\varLambda_b^0$  decay respectively. Appendix E contains the results for Gaussian widths of  $\sigma = 3 \,\mathrm{MeV}/c^2$  and  $\sigma = 10 \,\mathrm{MeV}/c^2$  with appropriately scaled selection windows.

Figure 10 shows how the level of contamination to each of the three fully visible decays changes for different time-of-flight resolution at CLD (top) and different time-of-flight resolution and cluster-counting efficiency at IDEA (bottom, including dN/dx information) in either case with and without the dE/dx measurement. The different colours represent the different decays where the initial differences in contamination between the decays predominantly stems from very different b-hadron hadronization fractions instead of differences in particle identification. Given the excellent resolution, the backgrounds can be suppressed to around or below 1% using only kinematic information. A further reduction in background at CLD by at least an order of magnitude

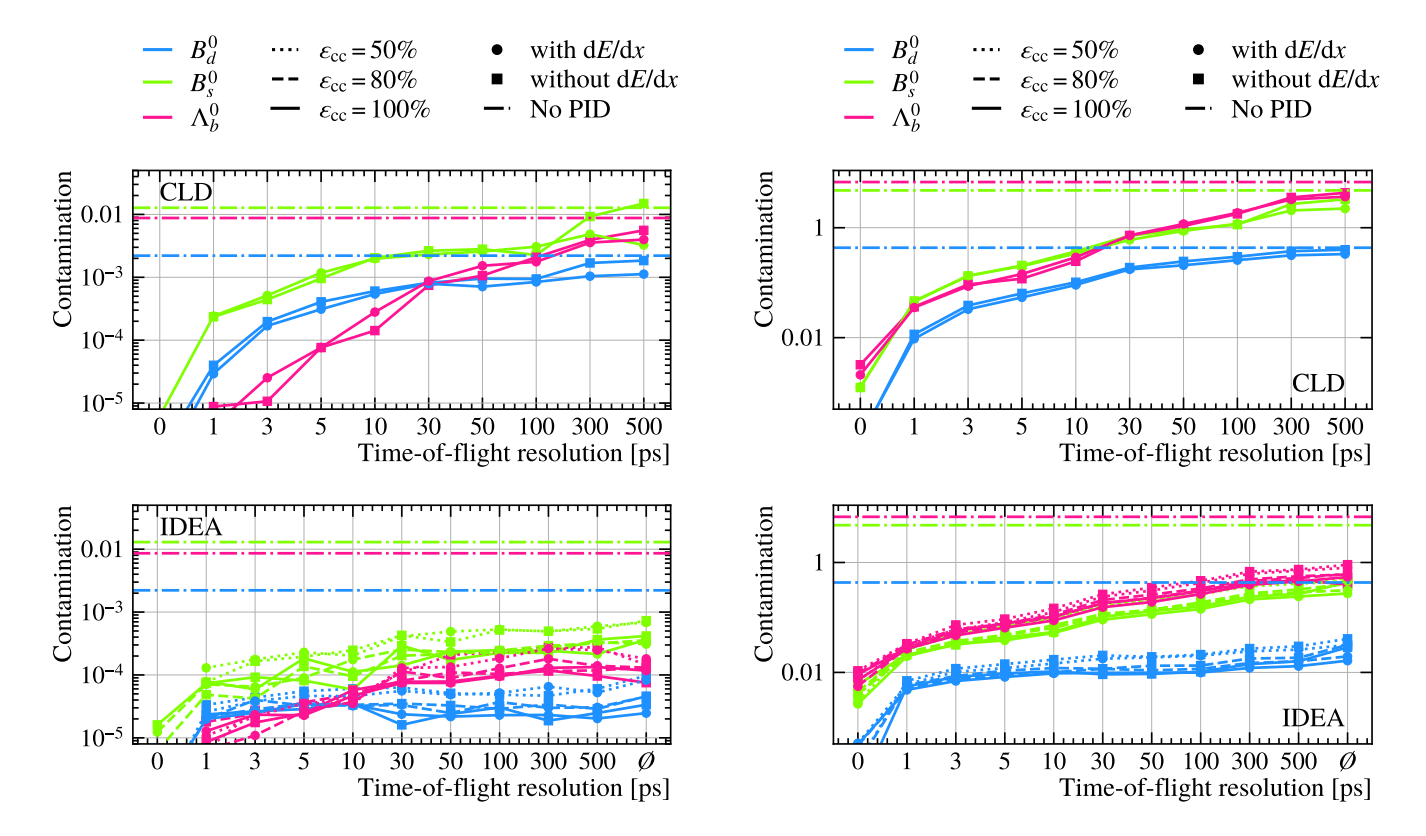


FIG. 10. Level of contamination for the three rare decays with fully visible final states (distinguished by colour) at (left/right) CLD and IDEA for different time-of-flight resolution (horizontal axis), different cluster-counting efficiencies  $\varepsilon_{cc}$  (IDEA only, distinguished by linestyle), and with or without using energy-deposit information from the silicon sensors (markerstyle). The four-body invariant masses are smeared using a Gaussian of width  $\sigma=5\,\mathrm{MeV}/c^2$  with signal window and background vetoes of  $\pm 10\,\mathrm{MeV}/c^2$ .

FIG. 11. Level of contamination for the three rare decays with semi-visible final states (distinguished by colour) at (left/right) CLD and IDEA for different time-of-flight resolution (horizontal axis), different cluster-counting efficiencies  $\varepsilon_{cc}$  (IDEA only, distinguished by linestyle), and with or without using energy-deposit information from the silicon sensors (markerstyle). No selections on the four-body invariant-masses are applied.

would require time-of-flight resolution of 30-50 ps or better. Adding dE/dx information improves the particle identification only marginally and only for worse timeof-flight resolution. The right-most points in the IDEA plot (bottom) represent a configuration without time-offlight measurement revealing that the dN/dx information on its own can reduce the contamination by over one order of magnitude wrt. no particle identification (dashdotted lines). The cluster-counting efficiency as well as including a dE/dx measurement has limited impact. Additional time-of-flight information improves on a purely dN/dx-based classifier by an order of magnitude for resolutions below 10 ps. Note that the strong fluctuations between the different points at very low contamination values are a consequence of the strong background suppression leaving only a small fraction of the 1 000 000 generated decays per species.

All these observations are a consequence of the momentum spectrum shown in Fig. 8 and agree with the discussions in Sec. III. The particles have momenta that are small enough to benefit from moderate time-of-flight

resolution (at least 30–50 ps at CLD). At the same time, many particles have momenta that are large enough to avoid the region of intersecting dN/dx curves such that a dN/dx measurement on its own provides strong classification that can only be improved with excellent time-of-flight resolution below 10 ps.

In conclusion, the benefit of particle identification for fully-visible rare-decay measurements is limited due to the excellent four-body invariant-mass resolution at all FCC-ee detectors leading to almost negligible amounts of background. The practical improvement in contamination however might allow for a background-free analysis with negligible associated systematic uncertainty. Because the contribution of New Physics can vary across the dimuon invariant-mass squared,  $q^2$ , App. E provides the level of contamination in bins of  $q^2$  for a time-of-flight resolution of 30 ps and a cluster-counting efficiency of 80%.

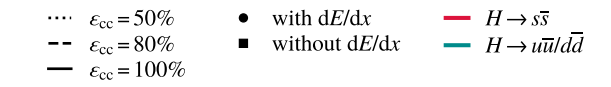
#### 2. Final-states with neutrinos

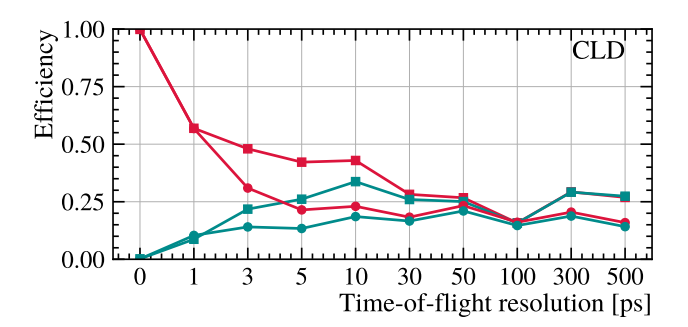
For semi-visible decays such as  $H_b \to h_1^+ h_2^- \nu_\ell \overline{\nu}_\ell$ , no windows around the signal and background masses can be defined leading to contaminations that are three orders of magnitude larger than in the fully-visible case. Figure 11 shows the resulting contamination without the kinematic selections. The improvements achieved through particle identification are of similar magnitude as in the fullyvisible case. As a consequence, the contamination to  $B^0$ decays can be suppressed to the percent level at IDEA almost independently of time-of-flight resolution. The improvement with better time-of-flight resolution is more marked for the other decays at IDEA and all decays at CLD. Note however that searches of these semi-visible final states as discussed in Ref. [55], would focus on individual dihadron resonance where additional kinematic selections suppress large amounts of misidentified backgrounds.

#### C. s-jet tagging

The FCC-ee provides unique opportunities for measurements involving a Higgs boson decaying to a pair of strange quarks. We study the impact of particle identification on s-jet tagging with simulation samples generated using Pythia assuming  $e^+e^-$  collisions at a center-ofmass energy of 240 GeV. Having a collision energy significantly above the ZH threshold maximises the production cross-section [56] and results in a momentum for each boson of around  $52 \,\text{GeV}/c$ . For the sake of this study, it is assumed that the final-state hadrons can be perfectly assigned to the Higgs or Z boson. Perfect assignment can be achieved either through anticipated advances in reconstruction tools in combination with the cleanliness of  $e^+e^-$  events and a non-zero boost of the Z and H bosons or by requiring that the Z boson decays to a dimuon pair, allowing unambiguous assignment of all seen hadrons to the Higgs boson at the cost of significantly reduced sample size.

Other  $H \to q\bar{q}$  and  $H \to gg$  decays present the most problematic backgrounds for  $H \to s\bar{s}$ . Taggers identifying jets from heavy quarks are very mature to date relying on high-dimensional information including in particular the long lifetime of b- and c-hadrons, see e.g. Refs. [57]. Gluon-jet tagging has been explored and often makes use of the significantly increased multiplicity and distinct shape of gluon-jets, see e.g. Refs. [58, 59], which study  $H \to s\overline{s}$  decays at the International Linear Collider. This work focuses on the distinction between s-jets and u-/d-jets. A simple but efficient proxy for the jet flavour in this case is the identity of the highestmomentum hadron as it likely stems from the original quarks produced in the Higgs decay. Based on the simulation produced for these studies, a pion carries most of the momentum in 80% of the u/d-jets. Only slightly above 10% of the u/d-jets result in a kaon with highest





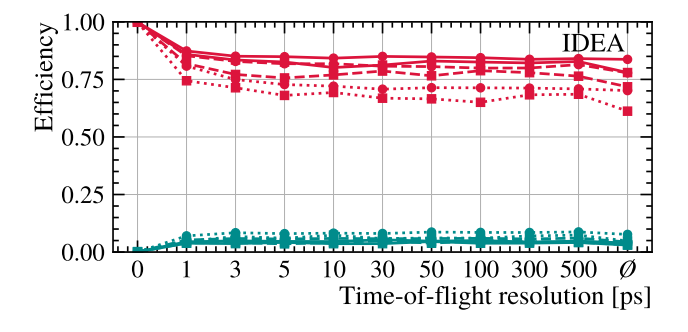


FIG. 12. Efficiency of tagging  $H \to u \overline{u}/d\overline{d}$  vs.  $H \to s\overline{s}$  based on whether the highest-momentum hadron in the jet is a kaon at (top/bottom) CLD and IDEA for different time-of-flight resolution (horizontal axis), different cluster-counting efficiencies  $\varepsilon_{\rm cc}$  (IDEA only, distinguished by linestyle), and with or without using energy-deposit information from the silicon sensors (markerstyle).

momentum. In s-jets on the other hand, pions and kaons are similarly likely to obtain the largest momentum at a rate of around 46%.

Figure 12 shows the efficiency of selecting events based on whether the particle with the highest momentum was a kaon. Note that the efficiency is calculated relative to the 46% (80%) of the  $H \to s\overline{s}$  ( $H \to u\overline{u}/dd$ ) events where the highest momentum particle was a kaon (pion). Due to the very high momenta shown in Fig. 8, CLD cannot easily distinguish the Higgs jets at realistic timeof-flight resolutions. The dE/dx information degrades the performance as it only adds noise in the high-momentum region without contributing discrimination power. Additional input from cluster-counting in the drift chamber at IDEA allows strong distinction between the jet flavours with a slight dependence on the cluster-counting efficiency. The trends described for IDEA agree with existing studies of more sophisticated flavour-tagging tools performed on fast simulation [58].

#### V. DISCUSSION

A study of the flavour capabilities of the CLD and IDEA detector concepts at the FCC-ee has been presented. The particle-identification algorithm used is based on three BDTs predicting a likelihood of a charged hadron to be a pion, kaon, or proton. The combination of  $\mathrm{d}N/\mathrm{d}x$  and moderate time-of-flight resolution results in a level of misidentification close to  $2\sigma$ , i.e. 2%, or better for a given particle combination across almost the entire momentum range appearing in  $e^+e^-\to Z\to b\bar{b}$  and  $e^+e^-\to ZH$  events, see Sec. III.  $\mathrm{d}E/\mathrm{d}x$  information may be useful at very low momentum but may deteriorate performance at very high momenta.

Three example physics studies are presented covering the low, medium, and high momentum regions. (A) Same-side flavour-tagging of  $B_s^0$  mesons relies on identification of very low momentum particles. In this region, good particle-identification can be achieved in almost all setups. In a classifier using only time-of-flight, a resolution of 30 ps or better is necessary to achieve the same performance as a purely dN/dx-based classifier. (B) Charged hadrons from rare b-decays sit in an intermediate momentum range. Here, the particles are still slow enough to benefit significantly from a time-of-flight measurement but require a resolution of at least 30–50 ps for notable improvements. A classifier relying exclusively on time-of-flight in this case would need perfect timeof-flight resolution in most cases (i.e. 0 ps) to achieve the same performance as a purely dN/dx-based classifier. (C) Tagging a Higgs jets based on the highest momentum hadron in the jet requires particle identification in the momentum range beyond  $10 \,\text{GeV}/c$ . A measurement of dN/dx in this case leads to solid performance while timeof-flight only provides useful additional information for vanishing resolution (i.e. 0 ps). In this particular case, the addition of dE/dx information to the time-of-flight measurement without dN/dx diluted the classification.

The three examples illustrate that flavour physics measurements do not necessarily require dedicated particle-identification detectors in order to achieve a passable level of background suppression. In some cases, a measurement of the time-of-flight suffices for solid background suppression. Moreover, a design including a drift chamber as part of the tracking system covers the full momentum range appearing in  $e^+e^- \to Z \to b\bar{b}$  and  $e^+e^- \to ZH$  events. It should be noted however that the selections used in the three examples are of an illustrative nature and the efficiencies and contaminations optimized for a specific more realistic analysis will differ to an extend.

Due to the lack of reconstruction software for the IDEA detector in this moment, the studies assume perfect reconstruction of the visible event as well as a uniform magnetic field when calculating the time-of-flight and flight distance. Neither assumption should have sizeable impact on the results presented in this publication. In contrast, the accuracy of the simulated dE/dx value might

not yet reflect a realistic level of noise. However the results of this study indicate that the particle identification does not rely heavily on the silicon-based dE/dx information. Neural networks and other more sophisticated machine-learning techniques as well as specific training samples might improve classification performance slightly in some cases without changing the observations made in this paper. Future investigations may consider realistic simulation of the cluster formation in the drift chamber that cover a potentially more complex cluster-counting efficiency as well as occupancy effects. Similarly, the inclusion of electrons and muons in the identification procedure and an extension of the classifier to calorimeter and muon chamber information could be of interest. Finally, the benefits to flavour-physics analyses in the presence of a dedicated particle-identification system should be ascertained in future studies.

#### ACKNOWLEDGEMENTS

We want to thank our colleagues in the FCC organisation for providing the software and advice, in particular Jan Eysermans and Brieuc Francois, as well as the participants in the *MIT and friends* FCC-ee meeting series for their discussion of this work. We would also like to acknowledge the US National Science Foundation, whose funding under award number 2310073 has helped support this work.

# Appendix A: Performance figures for different cluster-counting efficiencies at IDEA

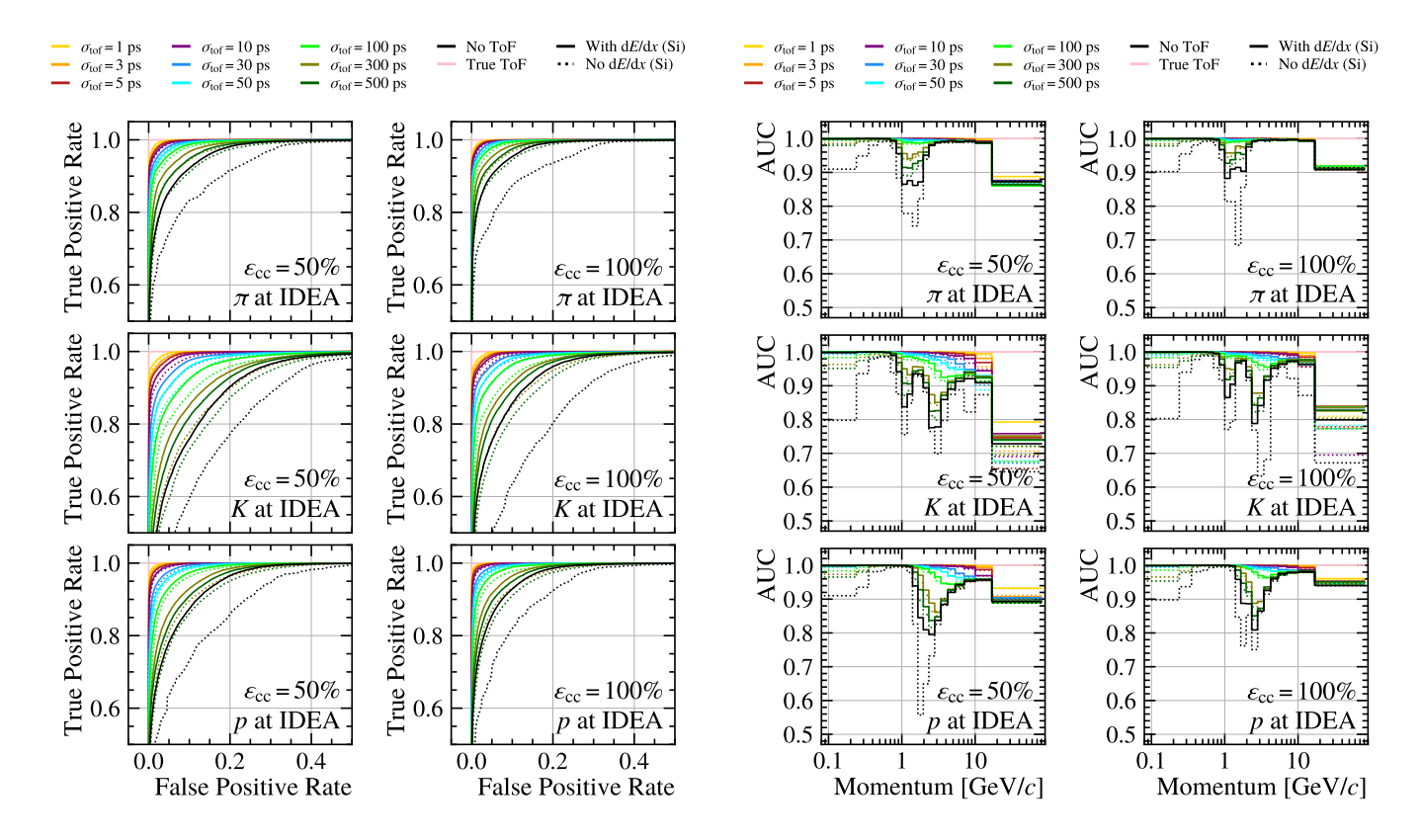


FIG. 13. (Left/right) ROC for the (top) pion, (middle) kaon, and (bottom) proton identification at IDEA with a cluster-counting efficiency  $\varepsilon_{\rm cc}$  of 50%/100%. The colours indicate the time-of-flight (ToF) resolution and the linestyle indicates whether the silicone-based dE/dx information was used.

FIG. 14. (Left/right) AUC in different momentum ranges for the (top) pion, (middle) kaon, and (bottom) proton identification at IDEA with a cluster-counting efficiency  $\varepsilon_{\rm cc}$  of 50%/100%. The colours indicate the time-of-flight (ToF) resolution and the linestyle indicates whether the silicone-based dE/dx information was used.

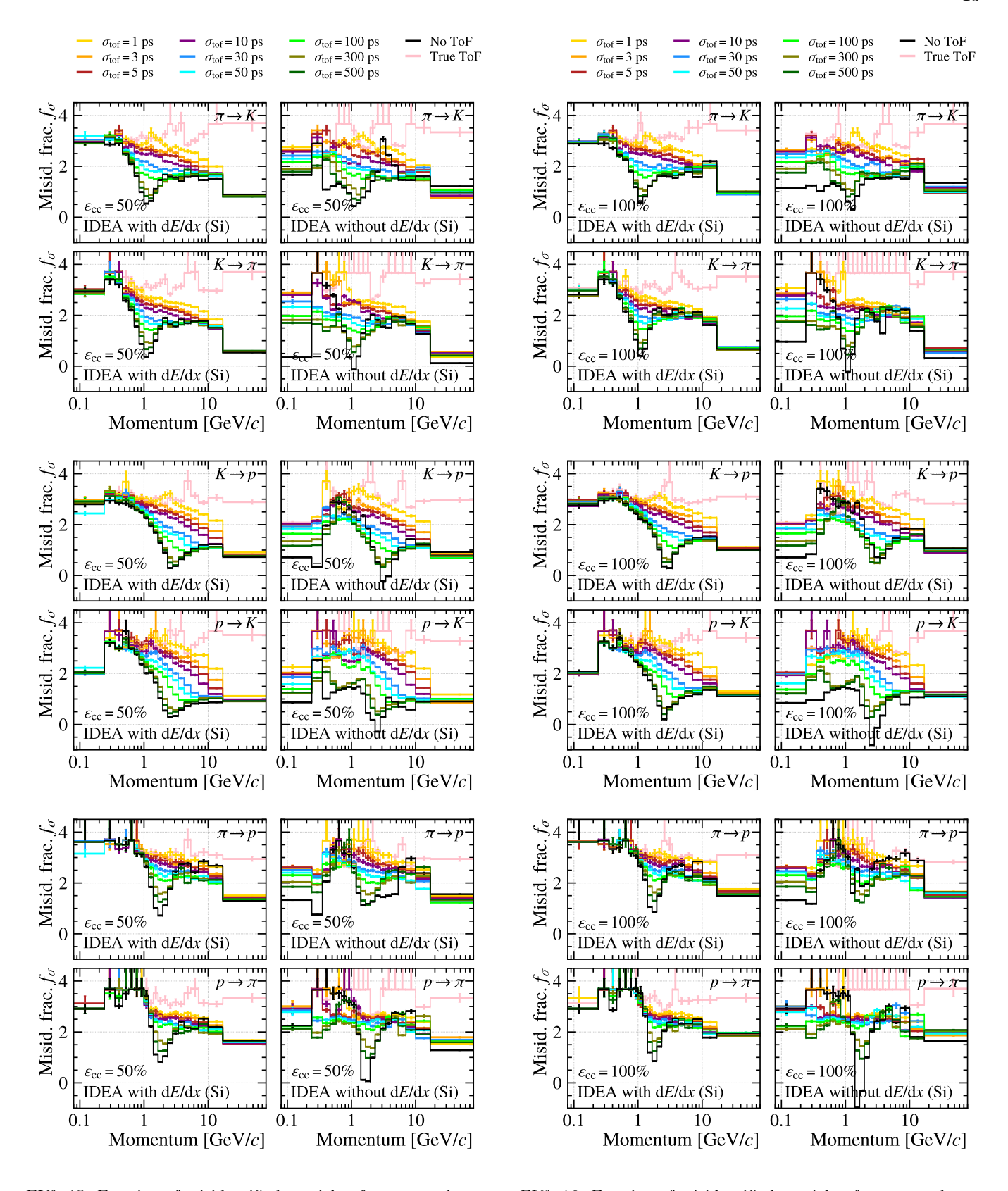


FIG. 15. Fraction of misidentified particles  $f_{\sigma}$  expressed as a number of standard deviations using Eq. (1) for each combination of hadron species (top, middle, bottom) for different time-of-flight resolution (ToF) without (left) and with (right) dE/dx information at IDEA (i.e.dN/dx measurement with or without time-of-flight and/or dE/dx measurement). A cluster-counting efficiency  $\varepsilon_{\rm cc}$  of 50% is assumed.

FIG. 16. Fraction of misidentified particles  $f_{\sigma}$  expressed as a number of standard deviations using Eq. (1) for each combination of hadron species (top, middle, bottom) for different time-of-flight resolution (ToF) without (left) and with (right) dE/dx information at IDEA (i.e.dN/dx measurement with or without time-of-flight and/or dE/dx measurement). A cluster-counting efficiency  $\varepsilon_{\rm cc}$  of 100% is assumed.

# Appendix B: BDT output scores

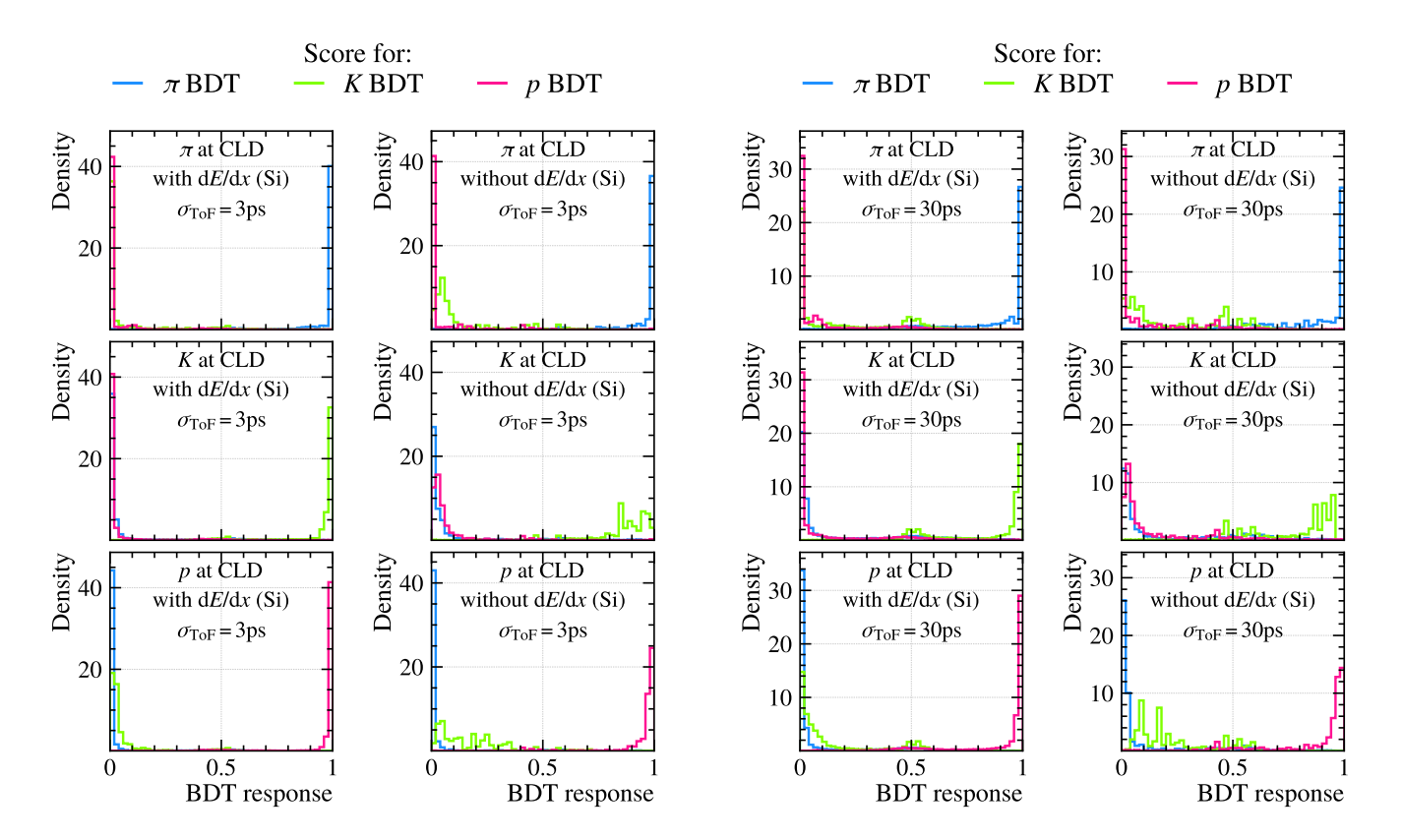


FIG. 17. (Left/right) Distribution of the BDT scores for a true (top) pion, (middle) kaon, and (bottom) proton at CLD for time-of-flight resolution of  $\sigma_{\text{ToF}} = 3 \, \text{ps}$  with/without silicone-based dE/dx measurement.

FIG. 18. (Left/right) Distribution of the BDT scores for a true (top) pion, (middle) kaon, and (bottom) proton at CLD for time-of-flight resolution of  $\sigma_{\text{ToF}}=30\,\text{ps}$  with/without silicone-based dE/dx measurement.

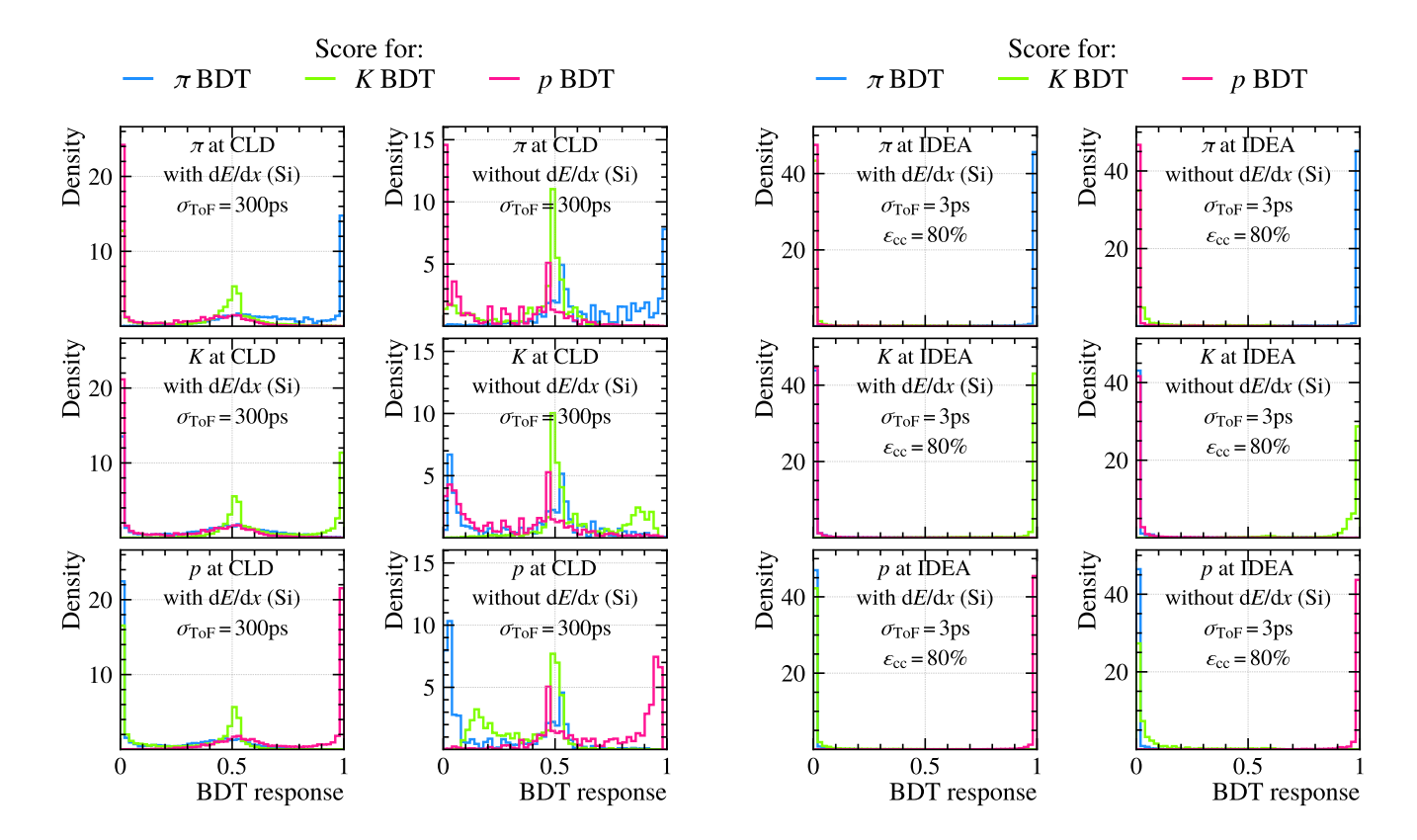


FIG. 19. (Left/right) Distribution of the BDT scores for a true (top) pion, (middle) kaon, and (bottom) proton at CLD for time-of-flight resolution of  $\sigma_{\rm ToF}=300\,{\rm ps}$  with/without silicone-based dE/dx measurement.

FIG. 20. (Left/right) Distribution of the BDT scores for a true (top) pion, (middle) kaon, and (bottom) proton at IDEA for time-of-flight resolution of  $\sigma_{\rm ToF}=3\,{\rm ps},$  cluster-counting efficiency of  $\varepsilon_{\rm cc}=80\%,$  with/without silicone-based dE/dx measurement.

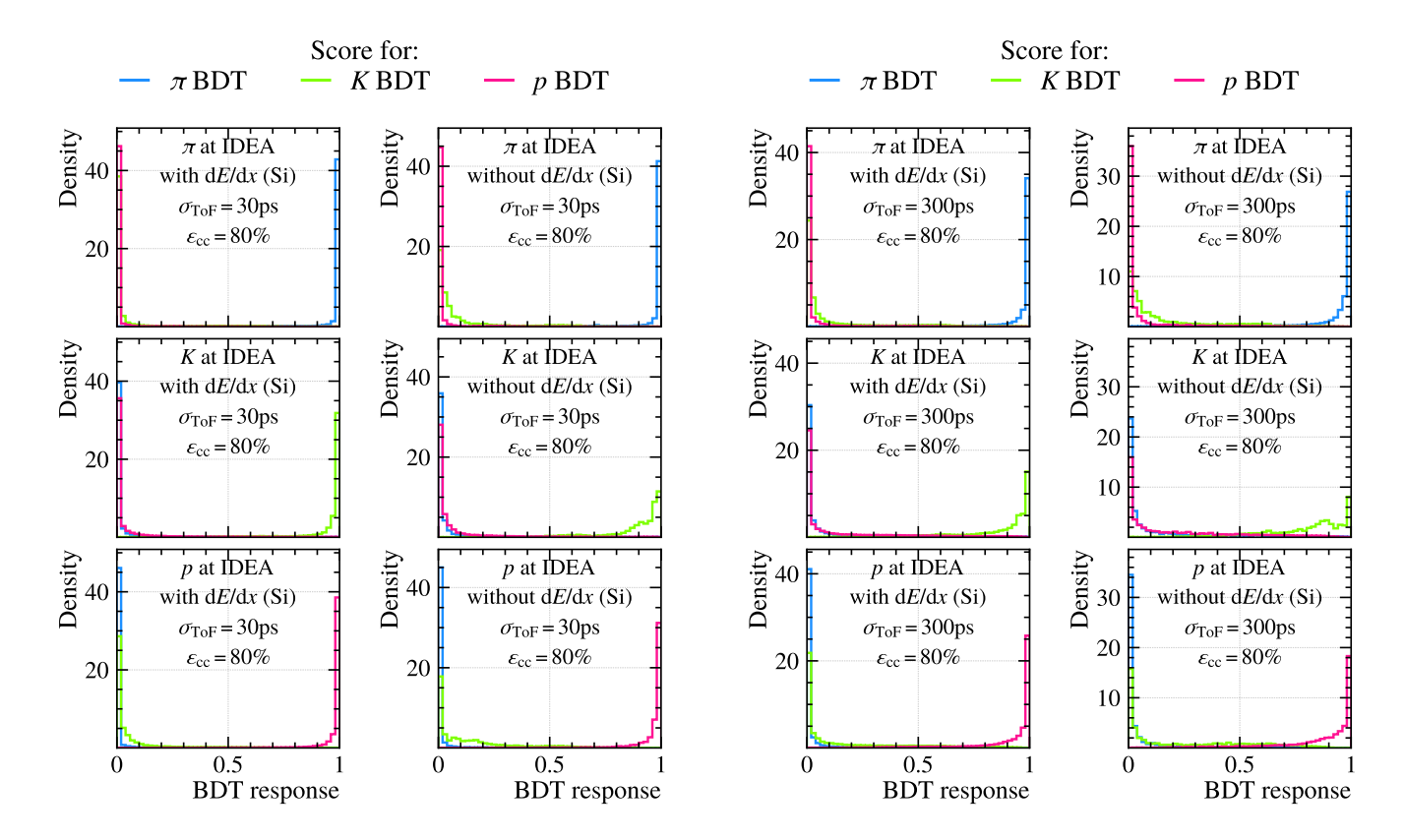


FIG. 21. (Left/right) Distribution of the BDT scores for a true (top) pion, (middle) kaon, and (bottom) proton at IDEA for time-of-flight resolution of  $\sigma_{\rm ToF}=30\,{\rm ps},$  cluster-counting efficiency of  $\varepsilon_{\rm cc}=80\%,$  with/without silicone-based dE/dx measurement.

FIG. 22. (Left/right) Distribution of the BDT scores for a true (top) pion, (middle) kaon, and (bottom) proton at IDEA for time-of-flight resolution of  $\sigma_{\text{ToF}} = 300 \, \text{ps}$ , cluster-counting efficiency of  $\varepsilon_{\text{cc}} = 80\%$ , with/without silicone-based dE/dx measurement.

#### Appendix C: Dihadron spectra

TABLE I. Individual resonances with their relative contribution to the decay rate as simulated in the dihadron spectra of the rare-decay studies.

Hadronic system	Resonance	Contribution
$B^0 \to K^- \pi^+$	$K^{*0}(892)$ $K^{*0}(1430)$	$0.850 \\ 0.150$
$B_s^0 \to K^- K^+$	$\begin{array}{ c c c } \hline \phi(1020) \\ f_2'(1525) \\ \hline \end{array}$	0.838 0.162
$\Lambda_b^0 \to pK^-$	$ \begin{array}{ c c } & A(1520) \\ & A(1600) \\ & A(1800) \\ & A(1820) \end{array} $	0.198 0.297 0.348 0.158

# Appendix D: Mass spread in rare decays

Figure 23 serves to illustrate the wide spread of misidentified rare decays when the signal decay is  $B_s^0 \to K^+ K^- \mu^+ \mu^-$ . The horizontal axis shows the value of the four-body invariant-mass reconstructed under the KK hypothesis for the dihadron system. The vertical axis corresponds to the momentum of either final-state hadron, such that every decay candidate is represented by two points in the figure. Correctly identified kaons in the  $B^0$  and  $A_b^0$  decays are shown as orange and dark blue points. They accumulate around the  $B_s^0$  mass but have a large spread. The yellow and lighter blue points on the other hand correspond to the pion and proton from the  $B^0$  and  $A_b^0$  decays if they were identified as kaons. Misidentification of a hadron with high momentum results in a four-body invariant-mass close to the truth, ie. the yellow (blue) points accumulate at the  $B_s^0$  ( $A_b^0$ ) mass. If the pion (proton) from a  $B^0$  ( $A_b^0$ ) decay has very low momentum and is misidentified as a kaon, the system artificially gains (looses) energy leading to increasingly high (low) four-body invariant-mass. In comparison to the background spread, the signal window of  $\pm 10 \, \text{GeV}/c^2$  is very narrow leading to efficient background suppression.

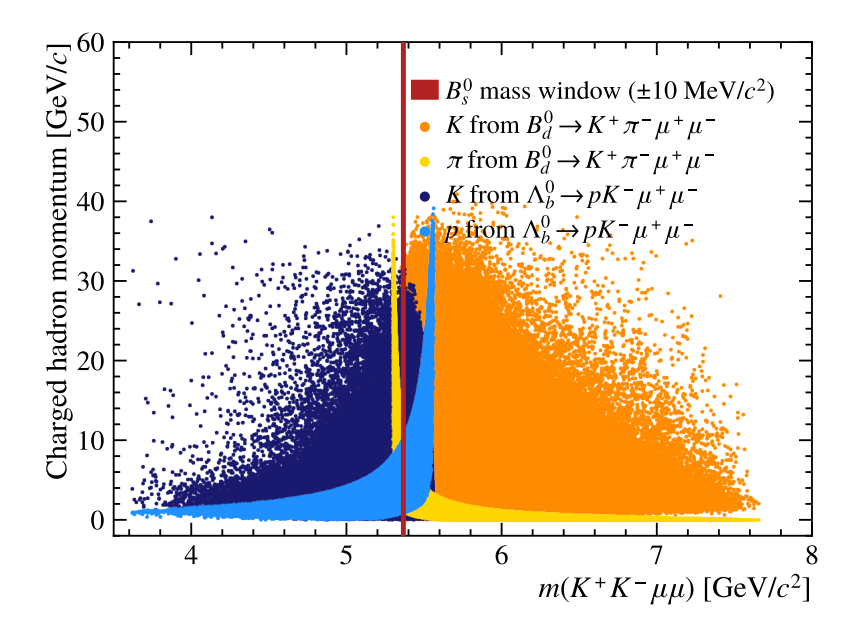


FIG. 23. Spread of the four-body invariant-mass for different hadron momenta in the case of correctly identified hadrons (red points, kaons from  $B^0$  and  $A_b^0$ ) and misidentified hadrons (yellow and blue points,  $\pi$  from  $B^0$  and p from  $A_b^0$ ).

# Appendix E: Contamination for different mass resolutions

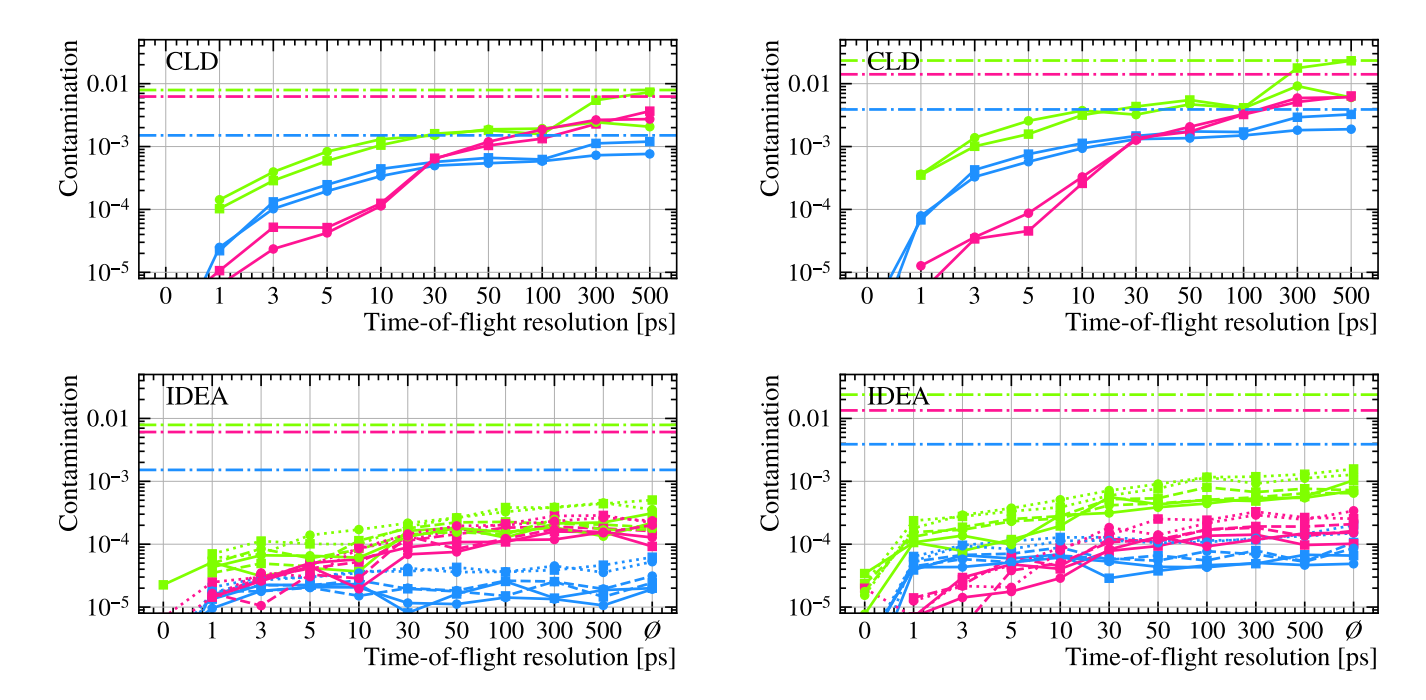


FIG. 24. Level of contamination for the three rare decays with fully visible final states (distinguished by colour) at (left/right) CLD and IDEA for different timing resolution (horizontal axis), different cluster-counting efficiencies (IDEA only, distinguished by linestyle), and with or without using energy-deposit information from the Silicon sensors (markerstyle). The four-body invariant masses are smeared using a Gaussian of width  $\sigma=3\,\mathrm{MeV}/c^2$  with signal window and background vetoes of  $\pm 6\,\mathrm{MeV}/c^2$ .

FIG. 25. Level of contamination for the three rare decays with fully visible final states (distinguished by colour) at (left/right) CLD and IDEA for different timing resolution (horizontal axis), different cluster-counting efficiencies (IDEA only, distinguished by linestyle), and with or without using energy-deposit information from the Silicon sensors (markerstyle). The four-body invariant masses are smeared using a Gaussian of width  $\sigma=10\,\mathrm{MeV}/c^2$  with signal window and background vetoes of  $\pm20\,\mathrm{MeV}/c^2$ .

#### Appendix F: Contamination in bins of the dimuon invariant-mass squared

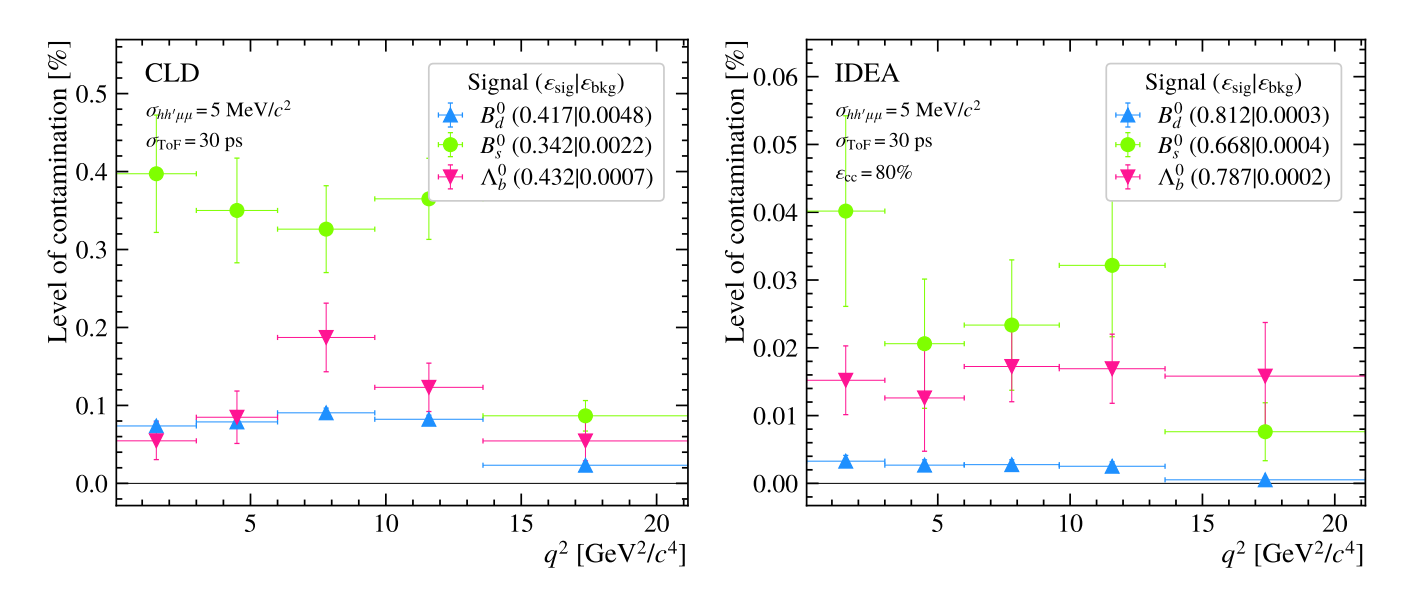


FIG. 26. Level of contamination across the dimuon invariant-mass squared assuming uniform  $q^2$  distributions for the fully visible final state. The time-of-flight resolution is  $\sigma_{\text{ToF}} = 30\,\text{ps}$  and the cluster-counting efficiency at IDEA is  $\varepsilon_{\text{cc}} = 80\%$ . The four-body invariant-mass is smeared using a Gaussian distribution with  $\sigma_{hh'\mu\mu} = 5\,\text{MeV}/c^2$ .

- M. Benedikt et al. (FCC), Future Circular Collider Feasibility Study Report: Volume 1, Physics, Experiments, Detectors (2025), arXiv:2505.00272 [hep-ex].
- W. Altmannshofer et al. (Belle-II), The Belle II Physics Book, PTEP 2019, 123C01 (2019), [Erratum: PTEP 2020, 029201 (2020)], arXiv:1808.10567 [hep-ex].
- [3] G. Viehhauser et al., Detectors in particle physics: a modern introduction (CRC Press, 2024).
- [4] R. Ricci, Study of maps silicon detector prototypes for the alice inner tracking system upgrade (2024).
- [5] N. Bacchetta *et al.*, CLD A Detector Concept for the FCC-ee (2019), arXiv:1911.12230 [physics.ins-det].
- [6] M. Abbrescia *et al.* (IDEA Study Group), The IDEA detector concept for FCC-ee (2025), arXiv:2502.21223 [physics.ins-det].
- [7] J. Pekkanen, ALLEGRO FCC-ee detector concept & Noble liquid calorimetry, Nuclear Instruments and Methods in Physics Research Section A: Accelerators, Spectrometers, Detectors and Associated Equipment 1069, 169921 (2024).
- [8] G. Ganis et al. (Key4hep), Key4hep, a framework for future HEP experiments and its use in FCC, Eur. Phys. J. Plus 137, 149 (2022), arXiv:2111.09874 [hep-ex].
- [9] K. Heijhoff et al., Timing performance of the lhcb velo timepix3 telescope, Journal of Instrumentation 15 (09), P09035.
- [10] A. Hayrapetyan et al. (CMS), Operation and performance of the CMS silicon strip tracker with proton-proton collisions at the CERN LHC (2025), arXiv:2506.17195 [physics.ins-det].

- [11] F. Cuna et al., Simulation of particle identification with the cluster counting technique, in *International Work-shop on Future Linear Colliders* (2021) arXiv:2105.07064 [physics.ins-det].
- [12] Track Momentum Resolution at LHCb in 2024 (2024).
- [13] S. Agostinelli *et al.* (GEANT4), GEANT4 A Simulation Toolkit, Nucl. Instrum. Meth. A **506**, 250 (2003).
- [14] J. Allison et al., Geant4 developments and applications, IEEE Trans. Nucl. Sci. 53, 270 (2006).
- [15] J. Allison et al., Recent developments in geant4, Nuclear Instruments and Methods in Physics Research Section A: Accelerators, Spectrometers, Detectors and Associated Equipment 835, 186 (2016).
- [16] FCC-config: Configuration files for the fcc event-processing chain (2025).
- [17] K. Collaboration, CLDConfig: Configuration repository for the cld detector model in the key4hep stack (2025).
- [18] T. Chen and C. Guestrin, Xgboost: A scalable tree boosting system, in Proceedings of the 22nd ACM SIGKDD International Conference on Knowledge Discovery and Data Mining, KDD '16 (ACM, 2016) p. 785–794.
- [19] R. Aaij *et al.* (LHCb), Updated measurement of time-dependent CP-violating observables in  $B_s^0 \rightarrow J/\psi K^+K^-$  decays, Eur. Phys. J. C **79**, 706 (2019), [Erratum: Eur.Phys.J.C 80, 601 (2020)], arXiv:1906.08356 [hep-ex].
- [20] R. Aaij et al. (LHCb), b flavour tagging using charm decays at the LHCb experiment, JINST 10 (10), P10005, arXiv:1507.07892 [hep-ex].
- [21] R. Aaij et al. (LHCb), New algorithms for identifying the flavour of  $B^0$  mesons using pions and protons, Eur. Phys.

- J. C 77, 238 (2017), arXiv:1610.06019 [hep-ex].
- [22] R. Aaij *et al.* (LHCb), A new algorithm for identifying the flavour of  $B_s^0$  mesons at LHCb, JINST **11** (05), P05010, arXiv:1602.07252 [hep-ex].
- [23] F. Abudinén et al. (Belle-II), b-flavor tagging at Belle II, Eur. Phys. J. C 82, 283 (2022), arXiv:2110.00790 [hep-ex].
- [24] A. Hayrapetyan *et al.* (CMS), Angular analysis of the  $B^0 \to K^{*0}(892)\mu^+\mu^-$  decay in proton-proton collisions at  $\sqrt{s}=13$  TeV, Phys. Lett. B **864**, 139406 (2025), arXiv:2411.11820 [hep-ex].
- [25] S. Wehle *et al.* (Belle), Lepton-flavor-dependent angular analysis of  $B \to K^* \ell^+ \ell^-$ , Phys. Rev. Lett. **118**, 111801 (2017), arXiv:1612.05014 [hep-ex].
- [26] M. Aaboud *et al.* (ATLAS), Angular analysis of  $B_d^0 \to K^* \mu^+ \mu^-$  decays in pp collisions at  $\sqrt{s}=8$  TeV with the ATLAS detector, JHEP **10**, 047 (2018), arXiv:1805.04000 [hep-ex].
- [27] R. Aaij et al. (LHCb), Measurement of *CP*-averaged observables in the  $B^0 \to K^{*0} \mu^+ \mu^-$  decay, Phys. Rev. Lett. **125**, 011802 (2020), arXiv:2003.04831 [hep-ex].
- [28] R. Aaij *et al.* (LHCb), Differential branching fraction and angular analysis of the decay  $B_s^0 \to \phi \mu^+ \mu^-$ , JHEP **07**, 084 (2013), arXiv:1305.2168 [hep-ex].
- [29] R. Aaij *et al.* (LHCb), Angular analysis and differential branching fraction of the decay  $B_s^0 \to \phi \mu^+ \mu^-$ , JHEP **09**, 179 (2015), arXiv:1506.08777 [hep-ex].
- [30] R. Aaij et al. (LHCb), Branching fraction measurements of the rare  $B_s^0 \to \phi \mu^+ \mu^-$  and  $B_s^0 \to f_2'(1525)\mu^+ \mu^-$  decays, Phys. Rev. Lett. **127**, 151801 (2021), arXiv:2105.14007 [hep-ex].
- [31] R. Aaij *et al.* (LHCb), Differential branching fractions and isospin asymmetries of  $B^0 \to K^{(*)} \mu^+ \mu^-$  decays, JHEP **06**, 133 (2014), arXiv:1403.8044 [hep-ex].
- [32] R. Aaij *et al.* (LHCb), Angular analysis of the  $B^+ \to K^{*+} \mu^+ \mu^-$  decay, Phys. Rev. Lett. **126**, 161802 (2021), arXiv:2012.13241 [hep-ex].
- [33] R. Aaij *et al.* (LHCb), Amplitude analysis of the  $B^0 \to K^{*0} \mu^+ \mu^-$  decay, Phys. Rev. Lett. **132**, 131801 (2024), arXiv:2312.09115 [hep-ex].
- [34] R. Aaij *et al.* (LHCb), Comprehensive analysis of local and nonlocal amplitudes in the  $B^0 \to K^{*0} \mu^+ \mu^-$  decay, JHEP **09**, 026 (2024), arXiv:2405.17347 [hep-ex].
- [35] A. Hayrapetyan et al. (CMS), Test of lepton flavor universality in  $B^{\pm} \to K^{\pm} \mu^{+} \mu^{-}$  and  $B^{\pm} \to K^{\pm} e^{+} e^{-}$  decays in proton-proton collisions at  $\sqrt{s} = 13 \text{ TeV}$ , Rept. Prog. Phys. 87, 077802 (2024), arXiv:2401.07090 [hep-ex].
- [36] J. P. Lees *et al.* (BaBar), Measurement of branching fractions and rate asymmetries in the rare decays  $B \to K^{(*)} \ell^+ \ell^-$ , Phys. Rev. **D86**, 032012 (2012), arXiv:1204.3933 [hep-ex].
- [37] S. Choudhury *et al.* (Belle), Test of lepton flavor universality and search for lepton flavor violation in  $B \to K\ell\ell$  decays, JHEP **03**, 105 (2021), arXiv:1908.01848 [hep-ex].
- [38] R. Aaij *et al.* (LHCb), Test of lepton universality using  $B^+ \to K^+ \ell^+ \ell^-$  decays, Phys. Rev. Lett. **113**, 151601 (2014), arXiv:1406.6482 [hep-ex].
- [39] R. Aaij *et al.* (LHCb), Test of lepton universality with  $B^0 \to K^{*0} \ell^+ \ell^-$  decays, JHEP **08**, 055 (2017), arXiv:1705.05802 [hep-ex].

- [40] R. Aaij et al. (LHCb), Test of lepton universality using  $\Lambda_b^0 \to p K^- \ell^+ \ell^-$  decays, JHEP **05**, 040 (2020), arXiv:1912.08139 [hep-ex].
- [41] R. Aaij et al. (LHCb), Test of lepton universality in beauty-quark decays, Nature Physics 18, 277 (2022), arXiv:2103.11769 [hep-ex].
- [42] R. Aaij *et al.* (LHCb), Tests of lepton universality using  $B^0 \to K_S^0 \ell^+ \ell^-$  and  $B^+ \to K^{*+} \ell^+ \ell^-$  decays, Phys. Rev. Lett. **128**, 191802 (2022), arXiv:2110.09501 [hep-ex].
- [43] R. Aaij *et al.* (LHCb), Measurement of lepton universality parameters in  $B^+ \to K^+ \ell^+ \ell^-$  and  $B^0 \to K^{*0} \ell^+ \ell^-$  decays, Phys. Rev. **D108**, 032002 (2023), arXiv:2212.09153 [hep-ex].
- [44] R. Aaij et al. (LHCb), Test of lepton universality in  $b \rightarrow s \ell^+ \ell^-$  decays, Phys. Rev. Lett. **131**, 051803 (2023), arXiv:2212.09152 [hep-ex].
- [45] T. Sjöstrand et al., An introduction to PYTHIA 8.2, Comput. Phys. Commun. 191, 159 (2015), arXiv:1410.3012 [hep-ph].
- [46] D. J. Lange, The EvtGen particle decay simulation package, Nucl. Instrum. Meth. A 462, 152 (2001).
- [47] R. Aaij et al. (LHCb), Amplitude analysis of the radiative decay  $B_s^0 \to K^+K^-\gamma$ , JHEP **08**, 093, arXiv:2406.00235 [hep-ex].
- [48] R. Aaij et al. (LHCb), Amplitude analysis of the  $A_b^0 \to pK^-\gamma$  decay, JHEP **06**, 098, arXiv:2403.03710 [hep-ex].
- [49] K. Chilikin *et al.* (Belle), Observation of a new charged charmoniumlike state in  $\bar{B}^0 \to J/\psi K^-\pi^+$  decays, Phys. Rev. **D90**, 112009 (2014), arXiv:1408.6457 [hep-ex].
- [50] Y. S. Amhis *et al.* (HFLAV), Averages of b-hadron, c-hadron, and  $\tau$ -lepton properties as of 2018, Eur. Phys. J. C **81**, 226 (2021), arXiv:1909.12524 [hep-ex].
- [51] H.-Y. Jiang and F.-S. Yu, Fragmentation-fraction ratio  $f_{\Xi_b}/f_{A_b^0}$  in *b* and *c*-baryon decays, Eur. Phys. J. C **78**, 224 (2018), arXiv:1802.02948 [hep-ph].
- [52] T. H. Kwok *et al.*, Time-Dependent Precision Measurement of  $B_s^0 \to \phi \mu^+ \mu^-$  Decay at FCC-ee (2025), arXiv:2506.08089 [hep-ph].
- [53] A. Beck *et al.*, Constraints on New Physics from decays of polarized  $\Lambda_b^0$  baryons at the FCC-ee (2025), arXiv:2510.02225 [hep-ex].
- [54] A. Di Canto et al., New opportunities for rare charm from  $Z \to c\overline{c}$  decays (2025), arXiv:2509.10447 [hep-ph].
- [55] Y. Amhis *et al.*, Prospects for searches of  $b \to s\nu_\ell \overline{\nu}_\ell$  decays at FCC-ee, JHEP **01**, 144, arXiv:2309.11353 [hep-ex].
- [56] M. Dong et al. (CEPC Study Group), CEPC Conceptual Design Report: Volume 2 - Physics & Detector (2018), arXiv:1811.10545 [hep-ex].
- [57] H. Abidi et al., FCC feasibility studies: Impact of trackerand calorimeter-detector performance on jet flavor identification and Higgs physics analyses, Phys. Rev. D 112, 052002 (2025), arXiv:2504.11103 [hep-ex].
- [58] F. Bedeschi et al., Jet flavour tagging for future colliders with fast simulation, Eur. Phys. J. C 82, 646 (2022), arXiv:2202.03285 [hep-ex].
- [59] A. Albert et al., Strange quark as a probe for new physics in the Higgs sector, in Snowmass 2021 (2022) arXiv:2203.07535 [hep-ex].